JOURNAL OF SPACECRAFT AND ROCKETS
Vol. 37, No. 5, September–October 2000

Trajectory Optimization for a Missile Using a Multitier Approach

Craig A. Phillips* and June C. Drake†
U.S. Naval Surface Warfare Center, Dahlgren, Virginia 22448

A two-tier approach to the midcourse trajectory design for a surface-to-air missile to maximize the probability of hit is presented. The first tier represents the midcourse trajectory of the missile, and the second tier represents the terminal homing phase. The first-tier trajectory is optimized with an auxiliary constraint on the value of the approach angle to the intercept at handover to the terminal phase. The handover approach angle is used as the governing parameter in generating a field of optimum first-tier midcourse trajectories. The second-tier model estimates the probability of hit including a full suite of stochastic error sources on the seeker and missile. The optimal approach angle and midcourse trajectory are demonstrated to be dependent on the terminal homing noise contributors and the target maneuver.

Nomenclature

A_e	=	exit plane area of the second stage motor, ft^2
a_{bo}	=	burnout acceleration compensation term in terminal guidance, ft/s^2
a_c	=	commanded missile external specific force normal to the body, ft/s^2
$a\,\text{norm}_{1,2}$	=	scaling factor for constraints
a_T	=	target acceleration, ft/s^2
a_{xB}, a_{zB}	=	missile external specific forces along body frame axes, ft/s^2
a_{zW}	=	missile external specific forces along the z wind axis, ft/s^2
C_A	=	axial force coefficient
C_{D0}	=	zero-angle-of-attackdrag coefficient at sea level
C_L	=	lift coefficient
$C_{L\max}$	=	maximum lift coefficient for the airframe
D	=	missile drag force, lb
E	=	missile specific energy (relative to launch inertial frame), ft
E_I	=	missile specific energy (relative to launch inertial frame) at end of first stage, ft
g_i	=	first-tier constraint vector element
g_{xW}, g_{zW}	=	local gravity acceleration along wind system axes, ft/s^2
g_0	=	reference gravitational acceleration, 32.2 ft/s^2
h_{loc}	=	local missile altitude above the Earth, ft
K	=	drag due to lift factor
K_g	=	guidance gain
m	=	missile mass, slug
p, p_{sl}	=	atmospheric pressure at altitude and at sea level, lb/ft^2
q	=	dynamic pressure, lb/ft^2
$q_{\min}$	=	minimum dynamic pressure during the midcourse flight, lb/ft^2
R_e	=	Earth radius, 20,926,218 ft
R_{mt}	=	range from missile to target, ft
$\boldsymbol{R}_{\text{mt}}$	=	relative position vector of missile to target, ft
R_{ST}	=	range from fire control platform to target, ft
r_{bes}	=	boresight error slope
S_{ref}	=	aerodynamic reference area, ft^2
T, T_{sl}	=	missile thrust force and thrust at sea level, lb
T_{man}	=	time of target maneuver relative to missile handover time, s
t	=	flight time, s
V	=	missile velocity, ft/s
$\boldsymbol{V}_{\text{mt}}$	=	relative velocity vector of missile and target, ft/s
x, z	=	missile position in launch inertial frame coordinates, ft
x_{PIP}, z_{PIP}	=	predicted intercept point (PIP) in launch inertial frame coordinates, ft
x_T, z_T	=	target position in launch inertial frame coordinates, ft
α	=	angle of attack, rad
$\alpha_{\max}$	=	maximum angle of attack, rad
α_N	=	noise filter gain
β	=	semiactive bistatic angle, rad
γ	=	angle between missile velocity vector and the launch inertial frame x axis, rad
$\dot{\gamma}$	=	flight-path angle rate relative to launch inertial frame, rad/s
$\tilde{\dot{\gamma}}$	=	flight-path angle rate relative to launch inertial frame for constant cruise altitude, rad/s
$\dot{\gamma}_{\text{com}}$	=	commanded missile flight-path angle rate relative to launch inertial frame x axis, rad
ΔC_{DA}	=	drag coefficient delta due to angle of attack
ΔC_{DB}	=	base drag coefficient delta due to motor operation
ΔC_{Dh}	=	drag coefficient delta due to altitude
ΔC_L	=	violation of maximum C_L constraint
δt	=	missile guidance update period, s
$\varepsilon_{\text{meas}}$	=	measured target boresight angle, rad
η_{bs}	=	boresight error angle induced by radome boresight error slope, rad
η_{glt}	=	boresight error angle induced by glint, rad
η_{rd}	=	boresight error angle induced by range-dependent receiver noise, rad
η_γ	=	uncontrolled variation on the heading error at handover due to noise, rad
θ_f	=	(approach angle) angle from inertial launch x axis to line of sight from missile to the PIP at handover, rad
θ_M	=	angle of missile body frame x axis relative to the launch inertial x axis, rad
θ_S	=	angle of missile seeker boresight relative to the launch inertial x axis, rad
θ_T	=	angle of line of sight from the missile to the target relative to the launch inertial x axis, rad
Λ	=	bistatic radar cross section factor
λ	=	seeker gimbal angle, rad
$\hat{\dot{\xi}}$	=	filtered measured seeker head rates, rad/s
σ_{he}	=	standard deviation of midcourse noise induced heading error at handover, rad
σ_{rd}	=	standard deviation of range-dependentangular noise, rad
τ_A	=	autopilot/airframe time constant, s
τ_N	=	noise filter time constant, s

Received 3 May 1999; revision received 1 June 2000; accepted for publication 19 June 2000.

*Lead Functional Design Engineer, Dahlgren Division, Missile Systems Division, 17320 Dahlgren Road. Senior Member AIAA.

†Program Manager, Dahlgren Division, Missile Systems Division, 17320 Dahlgren Road.

τ_s = seeker time constant, s
ϕ = angle between line of sight from missile to target and the target centerline, rad

Subscripts

ho = values at handover
I = values at end of first stage

Introduction

A MISSILE may have several guidance phases during its mission associated with the operation of different sensors. The sensors may be located on the missile or on a fire control platform. The guidance for each of these phases needs to be carefully designed in terms of contributing to the overall mission success. Each phase should place the missile at a set of states that allow the subsequent guidance phase to maximize the overall mission performance.

The midcourse guidance design of a two-stage surface-to-air missile with a command midcourse phase that transitions to a terminal semiactive radio frequency (rf) seeker guidance phase is considered in this paper. Figure 1 shows the sequential nature of the two guidance phases. The mission profile includes a first stage that operates in an open-loop manner to fly the missile from a vertical launch to a selected flight-path angle relative to the launch inertial frame. The midcourse phase represents the majority of the flyout. During the midcourse phase, the target track is provided by a surface-based radar located on a fire control platform. The measured target states are then broadcast to the interceptor via a communication link. Using the measured interceptor and target states, the missile generates guidance commands. Because of the ranges involved from the fire control radar to the target, relatively large targeting errors will be encountered.

To reduce the targeting errors as the missile approaches intercept, a semiactive rf seeker is carried onboard the missile. Although such a system has lower angular accuracy than a large surface-based radar, the shorter range from the missile to the target as the missile nears the intercept will decrease the final targeting errors. At the range to go to the intercept at which the missile-borne seeker provides lower targeting noise than the surface-based radar, the missile guidance handovers from midcourse to terminal guidance. During the terminal guidance, the semiactive rf seeker provides the target track. The elements of this command midcourse to semiactive rf seeker system are shown in Fig. 2.

The handover from one targeting process to another provides a convenient place to break the guidance design. For long-range intercepts, the midcourse phase is concerned with an efficient flight that satisfies the desired handover condition. Because the terminal guidance phase is relatively short, energy management is not of concern, and a guidance law such as proportional navigation is used.

A tiered approach to the design of the midcourse guidance is introduced in this paper to determine the set of handover states that optimize the overall performance. The performance of the intercept is measured by the probability of hit that is defined as the probability of passing through a 20-ft circle about the target geometric center. The probability of hit is determined by several factors. These include the target maneuver, the relative maneuverability of the target and missile, noises and biases on the missile instrument and seeker measurements, the time constant of the missile airframe, the residual heading error from the midcourse phase, and the geometry of the intercept set up at handover by the midcourse shaping. Except for the target maneuver, these factors are influenced through the midcourse trajectory shaping.

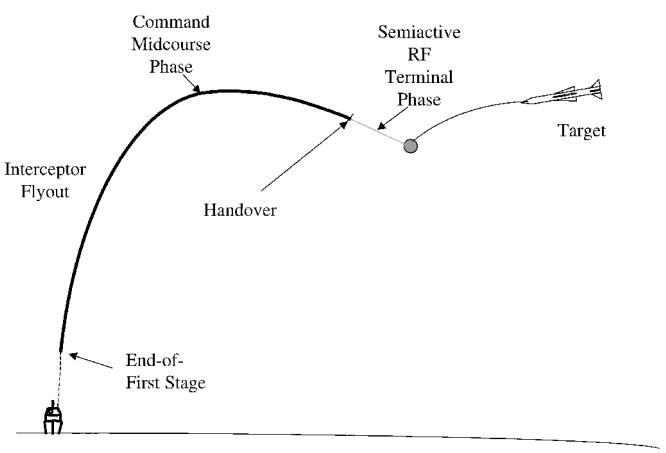

Fig. 1 Mission phases.

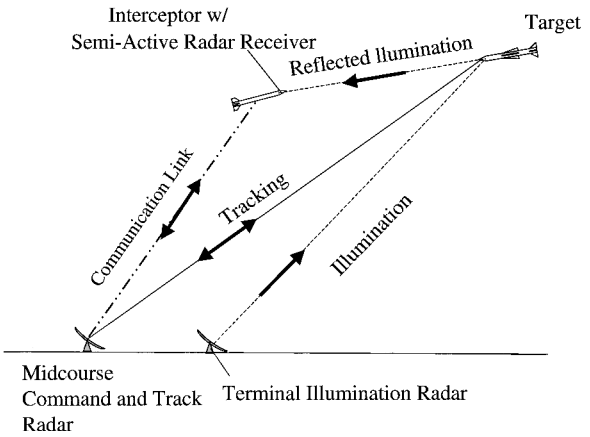

Fig. 2 System elements.

This paper optimizes the midcourse trajectory by the addition of an auxiliary constraint on the value of the approach angle to the midcourse trajectory design. The approach angle is defined at handover as the angle from the launch inertial x axis to the line of sight from the missile to the predicted intercept point (PIP). The approach angle was used as the governing parameter in generating a field of optimum first-tier trajectories. Significant differences in the midcourse shaping may be required to achieve different approach angles. The approach angle affects the missile states at handover including its position, speed, and maneuverability. The first tier includes the optimization algorithm and a two-degree-of-freedom point mass trajectory model. The second tier consists of a Monte Carlo terminal homing model with two-degree-of-freedom point mass dynamics and with an approximate first-order transfer function for the pitch dynamics. The second-tier model estimates the probability of hit of the missile.

The handover conditions for each set of trajectories are input to the second-tier terminal model. The probability of hit is computed for the handover conditions associated with each value of the approach angle constraint. Then the approach angle value that maximizes the probability of hit is the optimal solution.

The terminal homing of guided missiles has been extensively studied. The miss distances of missiles guided by proportional navigation due to target maneuvers, heading errors from midcourse phase navigation errors, receiver noise, and radome aberrations have been presented.[1–5] These efforts have yielded both numerical and closed-form solutions. Reference 6 has presented useful results for two target engagements. Reference 7 has examined the benefits of modifying the handover geometry achieved by the midcourse guidance to enhance the performance of terminal phase of an rf semiactive missile against multiple targets. That work did not include the midcourse phase performance penalties incurred to achieve the desired handover conditions.

Missile Description

The missile consists of two solid-propellant stages. A first booster stage burns for 8.3 s and pitches the missile over from a vertical launch to a selected flight path angle. A constant-thrust (as measured at sea level) motor powers the second stage. The interceptor is aerodynamically controlled by tail fins and includes a dorsal for increased lift effectiveness. The mass and thrust properties of the missile are given in Table 1.

Description of the First Tier

The first tier employs a two-degree-of-freedom model with trim aerodynamics coupled to an optimizer algorithm. The simulation is initialized at the end of the first stage and continues until the handover to the terminal guidance. The first-tier optimizer selects the flight-path angle relative to the launch inertial frame at the end of

Table 1 Missile description

Property	Value
Length	216 in.
Diameter	12 in. (upper stage) 15 in. (first stage)
Launch weight	2,772 lb
First-stage burnout weight	1,772 lb
Second-stage initial weight	1,470 lb
Second-stage burnout weight	873 lb
First-stage sea level thrust	30,000 lb (const)
First-stage burn time	8.3 s
Second-stage sea level thrust	7,164 lb (const)
Second-stage burn time	20 s

Table 2 End-of-first-stage conditions

γ_I, deg	x_I, ft	z_I, ft	V_I, ft/s
0.0	8,828	5,137	2,517
10	8,513	6,335	2,631
20	8,002	7,508	2,735
30	7,296	8,622	2,827
40	6,404	9,638	2,907
50	5,345	10,523	2,973
60	4,142	11,246	3,026
70	2,827	11,781	3,064
80	1,434	12,110	3,087
90	0	12,221	3,094

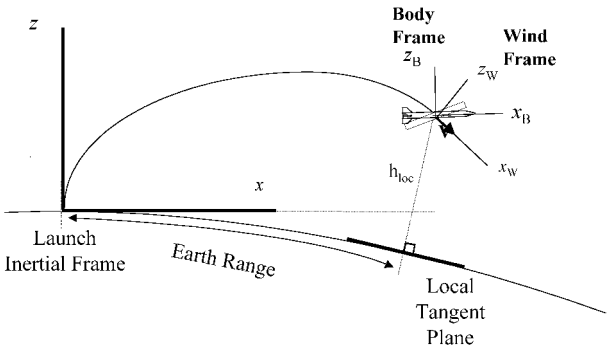

Fig. 3 Coordinate definitions.

the first stage, the control history, and the handover time to maximize the final specific energy of the missile at the handover to the terminal guidance phase of the flight. The optimization is subject to a number of constraints defined as part of the mission and the auxiliary approach angle constraint.

The first-tier dynamics are restricted to a single plane with the flight over a spherical Earth. Figure 3 shows the relationship of the launch inertial frame and its relationship to local altitude. The two position state variable equations in the launch inertial frame are

$$\dot{x} = V\cos(\gamma), \qquad \dot{z} = V\sin(\gamma) \tag{1}$$

The first-tier simulation is initialized at the end of the first stage. The position state variables are initialized at the position at the end of the fist tier. The values for the position and the missile velocity are obtained by interpolation with a cubic spline on the data in Table 2 as a function of the selected value of the end of first stage flight-path angle γ_I. Thus,

$$x(8.3) = x_I, \qquad z(8.3) = z_I \tag{2}$$

The third state variable equation is for the specific energy of the missile:

$$\dot{E} = \frac{[T\cos(\alpha) - D]V}{\text{weight}} \tag{3}$$

The velocity of the missile is determined from the specific energy of the missile and the local altitude such that

$$V = \sqrt{2g_0(E - h_{\text{loc}})} \tag{4}$$

The value of the local altitude as defined in Fig. 3 is found assuming a spherical Earth and using the two position states:

$$h_{\text{loc}} = \sqrt{R_e^2 + x^2 + z^2 + 2R_e z} - R_e \tag{5}$$

The initial value of the specific energy is obtained from

$$E_I = V_I^2/2g_0 + h_{\text{loc}I} \tag{6}$$

The final state is the flight-path angle that is defined as the angle of the missile velocity relative to the inertial launch frame x axis. The state variable equation for the flight-path angle is

$$\dot{\gamma} = \dot{\gamma}_{\text{com}} \tag{7}$$

The values of the commanded flight-path angle rate history are linearly interpolated in time between eight node points to yield the commanded flight-path angle rate. The first node is located at the time of the end of the first stage flight. The final node is located at the handover time t_{ho}. The remaining nodes are evenly spaced across the second stage flight time from the end of the first stage to the handover time. The commanded flight-path angle rate is given from linear interpolation by

$$\dot{\gamma}_{\text{com}} = f(\dot{\gamma}_1, \dot{\gamma}_2, \ldots, \dot{\gamma}_8) \tag{8}$$

The initial value of the flight-path angle at the initiation of the second stage is obtained from the selected parameter control vector:

$$\gamma(8.3) = \gamma_I \tag{9}$$

There are five constraints applied to the first-tier optimization problem. The first of these is the requirement that the missile's velocity vector be aligned with the selected approach angle at the handover point. The approach angle constraint is not defined as an element of the original problem but is used as a governing parameter to generate a field of optimal trajectories. This constraint is enforced as an equality constraint on the handover flight-path angle:

$$g_1 = \gamma_{\text{ho}} - \theta_f \tag{10}$$

The missile position and flight path at the handover time of the first-tier simulation, t_{ho}, must lie on a line emanating from the predicted intercept point along the selected approach angle. This requirement is enforced by two equality constraints on the position at handover. The handover to terminal guidance occurs when the estimated time to go to the predicted intercept point equals 10 s. The position constraints are defined as equality constraints and are scaled by the normalization factor $a\ \text{norm}_1$:

$$g_2 = \frac{x_{\text{ho}} - [x_{\text{PIP}} - 10V_{\text{ho}}\cos(\theta_f)]}{a\ \text{norm}_1}$$

$$g_3 = \frac{z_{\text{ho}} - [z_{\text{PIP}} - 10V_{\text{ho}}\sin(\theta_f)]}{a\ \text{norm}_1}$$

$$a\ \text{norm}_1 = 3500 \tag{11}$$

Two inequality constraints were imposed to satisfy the assumptions implicit in the trim aerodynamic model. The first of the inequality constraints restricts the minimum dynamic pressure during the flight. For dynamic pressure values greater than this value, the closed-loop airframe/autopilot is stable. The missile's dynamic pressure was not allowed to drop below a minimum of 120 lb/ft^2. The constraint is normalized by the variable $a\ \text{norm}_2$ for proper numerical scaling during the optimization process:

$$g_4 = \frac{q_{\min}/120 - 1}{a\ \text{norm}_2}, \qquad a\ \text{norm}_2 = 100 \tag{12}$$

The final constraint restricts the commanded flight path angle rate so that the resulting commanded load factors do not exceed the vehicle's capability. The maximum lift coefficient is determined by the missile trim lift coefficient resulting at the maximum angle of attack of 25 deg. This constraint is enforced through an integral-square penalty inequality constraint.[8] The implementation of this constraint is now presented.

The commanded missile external specific force along the z wind axis must include a gravity bias:

$$a_{zW} = V\dot{\gamma}_{\text{com}} + g_{zW} \tag{13}$$

The wind frame is defined in Fig. 3. The resulting lift coefficient is given by

$$C_L = \frac{a_{zW}\ \text{weight}}{qS_{\text{ref}}\ g_0} \tag{14}$$

The violation is given by

$$\Delta C_L = C_L - 0.95C_{L\max} \tag{15}$$

The constraint on the maximum lift coefficient is implemented so that the average violation is less than a value of 0.02:

$$g_5 = 1 - \frac{\int_{8.3}^{t_{\text{ho}}} \dot{E}_2\,\mathrm{d}t}{0.02(t_{\text{ho}} - 8.3)}, \qquad \dot{E}_2 = \Delta C_L^2 \quad \text{if} \quad \Delta C_L \geq 0$$

$$\dot{E}_2 = 0 \quad \text{if} \quad \Delta C_L < 0 \tag{16}$$

The first-tier optimization problems consisted of selecting the elements of the control vector that maximized the first-tier performance index. The parameters available for optimization include the end of the first stage flight-path angle γ_I relative to the launch inertial x axis, the flight-path angle rates ($\dot{\gamma}_1, \dot{\gamma}_2, \ldots, \dot{\gamma}_8$) at eight time node points, and the time of flight to the handover to terminal guidance t_{ho}. For the tiered approach, the first-tier performance index must be one that has a functional relationship to the probability of hit. Analysis with the second-tier Monte Carlo terminal phase model indicated that the probability of hit monotonically increases with the missile specific energy at handover when all other states are held constant.

The first-tier optimization problem is to select the control vector:

$$u^T = (\gamma_I, \dot{\gamma}_1, \dot{\gamma}_2, \dot{\gamma}_3, \dot{\gamma}_4, \dot{\gamma}_5, \dot{\gamma}_6, \dot{\gamma}_7, \dot{\gamma}_8, t_{\text{ho}}) \tag{17}$$

to maximize the performance index defined at the handover time,

$$J = E(t_{\text{ho}}) = V_{\text{ho}}^2 \big/ 2g_0 + h_{\text{loc ho}} \tag{18}$$

This solution is subject to the five constraints. The equality constraints are enforced as

$$g_i = 0 \tag{19}$$

Equations (10) and (11) define the three equality constraints. The two inequality constraints are implemented in the form

$$g_i \geq 0 \tag{20}$$

Equations (12) and (13) define the two inequality constraints.

Many numerical procedures exist to solve parameter optimization problems. The simplest procedures are the gradient or steepest-descent techniques. Second-order methods are also available to improve the rate of convergence, for example, the Newton–Raphson iteration, which requires the evaluation of the Hessian matrix. Quasi-Newton or variable-metric methods avoid the evaluation of the Hessian matrix by using iterative evaluation of first-order information to approximate the Hessian matrix. One such quasi-Newton method, the Broyden–Fletcher–Goldfarb–Shanno procedure, is implemented with constraint projection.[8]

Description of the Second Tier

The second-tier model is a Monte Carlo simulation that models the rf seeker noise, random target maneuvers, and the missile response. The missile is modeled as a two-degree point mass with an additional degree of freedom approximating the pitch dynamics as a first-order system. The missile includes an additional state variable for the seeker head dynamics and a first-order filter for the measured target boresight angles. The missile's roll motion is not modeled, but the body roll position is assumed constant. The target is modeled as a two-dimensional point mass and undergoes maneuvers in the pitch plane. Both the missile and the target are restricted to a plane above a spherical Earth.

Second-Tier Dynamics

The planar dynamics of the second-tier model also include two position states and two velocity states. The two position states are

$$\dot{x} = V\cos(\gamma), \qquad \dot{z} = V\sin(\gamma) \tag{21}$$

The values of the x and z are initialized by the handover values from the first-tier simulation:

$$x(t_{\text{ho}}) = x_{\text{ho}}, \qquad z(t_{\text{ho}}) = z_{\text{ho}} \tag{22}$$

The second-tier velocity dynamics are computed directly from the missile specific forces:

$$\dot{V} = a_{xB}\sin(\alpha) - a_{zB}\cos(\alpha) + g_{xW} \tag{23}$$

These specific forces are presented in the body frame as defined in Fig. 3. The velocity magnitude at handover from the first-tier model initializes this state for the second-tier model:

$$V(t_{\text{ho}}) = V_{\text{ho}} \tag{24}$$

The flight-path angle rate relative to the launch inertial frame is given by

$$\dot{\gamma} = [a_{xB}\sin(\alpha) + a_{zB}\cos(\alpha) + g_{zW}]/V \tag{25}$$

The flight-path angle is initialized at the value of the flight-path angle at handover from the first-tier model combined with an uncontrolled variation representing the noise sources during the first tier:

$$\gamma(t_{\text{ho}}) = \gamma_{\text{ho}} + \eta_\gamma \tag{26}$$

The component of external specific force along the missile body frame x axis is derived from the axial force coefficient:

$$a_{xB} = -qS_{\text{ref}}C_A/m \tag{27}$$

The axial force coefficient is computed as a function of the current angle of attack, Mach number, and the altitude. Appendix A describes the calculation of the axial force coefficient and the angle of attack.

The value of the specific external forces normal to the missile body is determined from the approximate model of the pitch dynamics. The state variable equation is

$$\dot{a}_{zB} = (a_c - a_{zB})/\tau_A \tag{28}$$

The value of the autopilot/airframe time constant τ_A is scheduled during the flight to maintain stability of the airframe in the presence of the radome boresight error slope. The scheduling process is presented in Appendix B. The initial value of a_{zB} is set based on the last value of the flight-path angle rate control vector from the first-tier trajectory:

$$a_{zB}(t_{\text{ho}}) = V_{\text{ho}}\dot{\gamma}_8 + g_{zW}(t_{\text{ho}}) \tag{29}$$

The seeker head dynamics are approximated as a first-order lag in response to the measured boresight angle of the target. The seeker head rate then becomes

$$\dot{\theta}_s = \varepsilon_{\text{meas}}/\tau_s \tag{30}$$

The seeker head time constant for this analysis was set at

$$\tau_s = 0.25\ \text{s} \tag{31}$$

The head rates are measured at 50 Hz and are then passed through a digital first-order filter:

$$\hat{\dot{\xi}}_i = \hat{\dot{\xi}}_{i-1} + \alpha_N(\dot{\theta}_s - \hat{\dot{\xi}}_{i-1}) \tag{32}$$

The noise filter gain is adaptively set during the flight so that the expected level of noise on the line-of-sight measurement (due to range-dependent noise and the target glint) does not induce commanded accelerations greater than one-half of the maximum lateral acceleration of the airframe. The initial value for the filtered head rate is set at handover:

$$\hat{\dot{\xi}}_{t_{\text{ho}}} = \hat{\dot{\xi}}_1 = 0 \tag{33}$$

The second-tier simulation includes target dynamics. The target is modeled as cruising at a constant speed at a constant local altitude

unless it is maneuvering. The target is modeled as having a constant speed regardless of maneuver. The maneuver acceleration is applied normal to the current target velocity vector. The target state variable equations are

$$\dot{x}_T = V_T \cos(\gamma_T), \qquad \dot{z}_T = V_T \sin(\gamma_T), \qquad \dot{\gamma}_T = a_T / V_T + \tilde{\dot{\gamma}} \tag{34}$$

The initial position of the target corresponds to a vehicle cruising at 3000 ft/s with 10 s time to go to the PIP:

$$x_T(t_{\text{ho}}) = 220531.0 \text{ ft}, \qquad z_T(t_{\text{ho}}) = 48841.0 \text{ ft}$$

$$\gamma_T(t_{\text{ho}}) = 0.01 \text{ rad} \tag{35}$$

The terminal guidance algorithm provides the control of the missile trajectory during the second tier. The algorithm consists of proportional navigation using the filtered seeker head rates from the digital first-order filter. The commanded specific external force along the missile body frame is given by

$$a_c = K_g \hat{\dot{\xi}} + a_{\text{bo}} + g_0 \cos(\theta_M) \tag{36}$$

The navigation gain K_g is defined as

$$K_g = -4 \frac{\dot{R}_{\text{mt}}}{\cos(\theta_M - \theta_S)} \tag{37}$$

The missile-to-target range rate $\dot{R}_{\text{mt}}$ is given by

$$\dot{R}_{\text{mt}} = \frac{\boldsymbol{V}_{\text{mt}} \cdot \boldsymbol{R}_{\text{mt}}}{R_{\text{mt}}} \tag{38}$$

The second term in Eq. (36) is a slowdown compensation term that corrects for guidance for the expected speed loss after the rocket motor burns out. The final term in Eq. (36) represents a gravity bias term expressed in terms of a body-fixed accelerometer implementation.

Second-Tier Noise Modeling

The second-tier model uses Monte Carlo techniques to determine the probability of hit. A number of noise sources are added to the simulation. These sources include errors on the measured boresight angle of the target due to glint, range-dependent receiver noise, and the uncompensated radome boresight error slope. Noises during the first tier are rolled up into a noise on the handover flight-path angle.

The measured boresight angle of the target is corrupted from the true value by noise. Then

$$\varepsilon_{\text{meas}} = \theta_T - \theta_s + \eta_{\text{glt}} + \eta_{\text{rd}} + \eta_{\text{bs}} \tag{39}$$

Should the magnitude of the gimbal angle exceed the limit of 45 deg, the seeker head rate is set to zero. The gimbal angle of the seeker is given by

$$\lambda = \theta_S - \theta_M \tag{40}$$

The value of the range-dependent noise induced error η_{rd} is determined from a zero mean white noise process with a standard deviation given by

$$\sigma_{\text{rd}} = 0.077 \Big/ \sqrt{\text{SNR}} \tag{41}$$

The signal-to-noise ratio (SNR) is a function of the radar cross section (RCS) of the target, the illumination power of the surface radar, and the intercept geometry. For this analysis, the SNR is given by

$$\text{SNR} = \frac{(2.0 \times 10^{21}) \text{RCS} \Lambda(\beta)}{R_{\text{mt}}^2 + R_{ST}^2} \tag{42}$$

The monostatic RCS is given by

$$\text{RCS} = 10.75 \text{ ft}^2 \tag{43}$$

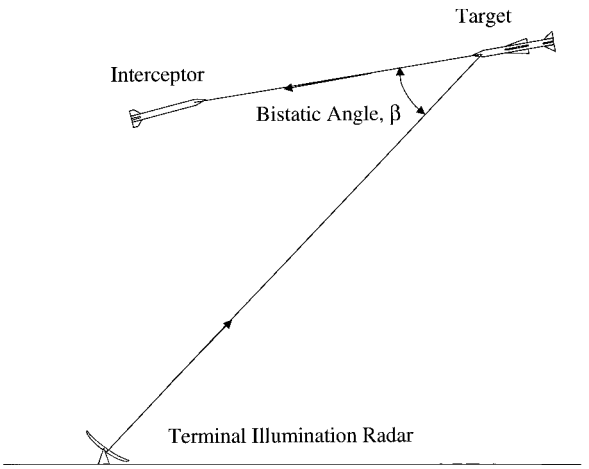

Fig. 4 Bistatic angle.

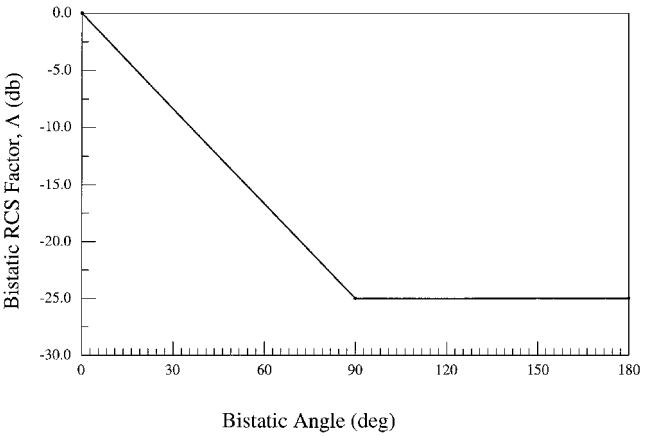

Fig. 5 Bistatic angle factor.

The bistatic RCS factor Λ determines the effective reduction in the monostatic RCS, as a function of the bistatic angle as defined in Fig. 4. The assumed bistatic RCS factor as a function of the bistatic angle is given in Fig. 5. The radar for used for the semiactive illumination during the terminal guidance is located on the fire control platform at the origin of the launch inertial frame. The range from fire control platform to target is given by

$$R_{ST} = \sqrt{x_T^2 + z_T^2} \tag{44}$$

During operation of the onboard rf seeker, refraction of the electromagnetic rays entering the missile radome cause the measured line-of-sight angle to the target to be in error proportional to the look angle between the true line of sight and the missile body axis. The uncompensated radome boresight error slope produces a boresight error of

$$\eta_{\text{bs}} = r_{\text{bes}}(\theta_T - \theta_m) \tag{45}$$

For each iteration of the second-tier model the radome error slope was drawn from a uniform distribution across a 0.08 deg/deg band with mean of zero.

The value of the target glint induced boresight error η_{glt} is determined by a zero mean white noise process. The standard deviation of the glint varied with viewing aspect of the target with a maximum value of 10 ft at an aspect angle of 90 deg:

$$\sigma_{\text{glt}} = \frac{10 \sin(\phi)}{R_{\text{mt}}} \tag{46}$$

Noise in the command midcourse phase from targeting and missile navigation errors is modeled as an uncontrolled variation on the handover fight-path angle used the initialize the second-tier model.

The value of the flight-path angle variation at handover, η_γ, is determined from a zero mean Gaussian distribution with a standard deviation of

$$\sigma_{he} = 2.0 \text{ deg} \tag{47}$$

Results

During the midcourse phase, the guidance flies the missile to a PIP. The midcourse trajectory was optimized using the tiered approach for a PIP located at launch inertial frame coordinates of (190,453, 49,132), which correspond to a range along the Earth's surface of 190,000 ft from the launch point and a local altitude of 50,000 ft. First, the trajectories are examined against a stationary target and PIP in the absence of targeting errors. Then the trajectories against a target maneuver after the initiation of the terminal phase are considered without system errors. The optimal approach angles are then determined under a variety of target maneuvers when the full system errors are considered.

A set of candidate optimal trajectories was created for approach angle constraint values from −30 to 90 deg. Steeper diving approach angles were not possible because of the constraints on the maximum lift coefficient for the airframe that were enforced during the first-tier optimization. Figure 6 shows the resulting midcourse trajectories from the first-tier optimization through the termination of the first-tier trajectory at the handover point. As the approach angle constraint value increases, the solution changes from the parabolic trajectory typical of maximum final velocity trajectories to the up-and-under trajectory shape. Figure 7 gives the optimizer-selected values of the flight-path angle at the end of the first stage. Sample histories of the optimized commanded flight-path angle rates are given in Fig. 8 for three approach angles. Table 3 shows the optimized time of flight to handover, the resulting handover positions in the launch inertial frame, and the resulting velocity at handover point for the 11 feasible first-tier trajectories.

Several things are noted from Fig. 6. First, the distance between the end of the midcourse trajectory and the PIP decreases as the approach angle increases and the handover speed decreases. Second, all of the trajectories have peak apogees that are higher than the final altitude. To conserve energy during the trajectory, it is necessary to get as high into the atmosphere as possible to reduce the form drag. This must be balanced off against the resulting maneuver drag associated with the harder turn for the higher apogee. The trajectories for the steeper positive approach angles have apogees higher than those for the shallower approach angles because the handover geometry places them in the lower atmosphere where the maneuver drag is decreased.

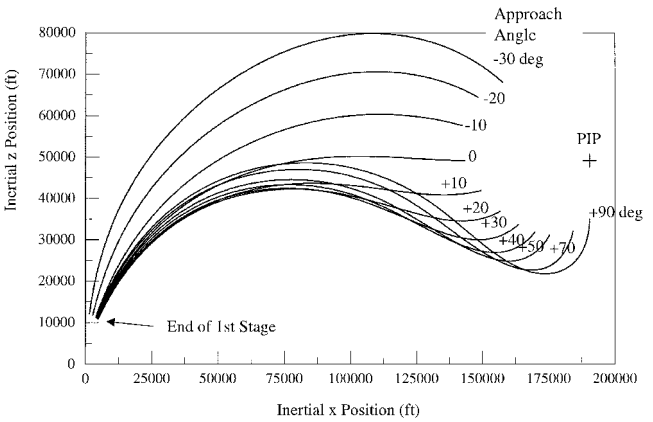

Fig. 6 First-tier (midcourse) optimal trajectories.

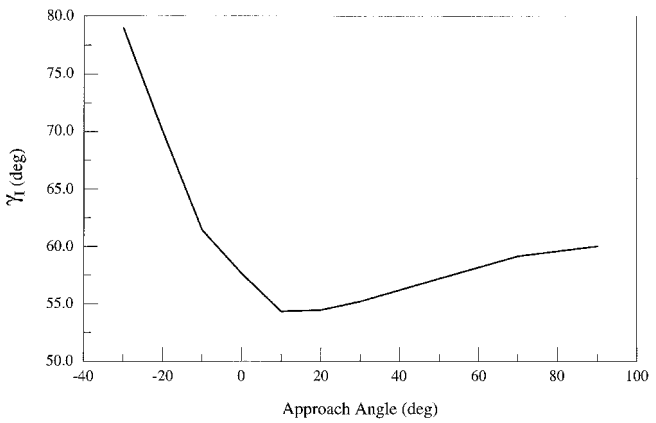

Fig. 7 Optimal end of first-stage flight-path angles.

Table 3 Handover conditions from tier 1

θ_f, deg	Time of flight, s	X_{ho}, ft	Z_{ho}, ft	V_{ho}, ft/s
−30	51.61	157,744	68,016	3,775
−20	45.84	148,397	64,439	4,474
−10	42.63	142,340	57,616	4,884
0	42.32	143,303	49,133	4,713
10	43.96	149,469	41,906	4,160
20	46.37	156,675	36,840	3,593
30	48.94	163,584	33,621	3,101
40	51.40	169,832	31,832	2,691
50	53.71	175,342	31,125	2,350
70	58.01	184,213	31,991	1,824
90	62.22	190,455	34,902	1,422

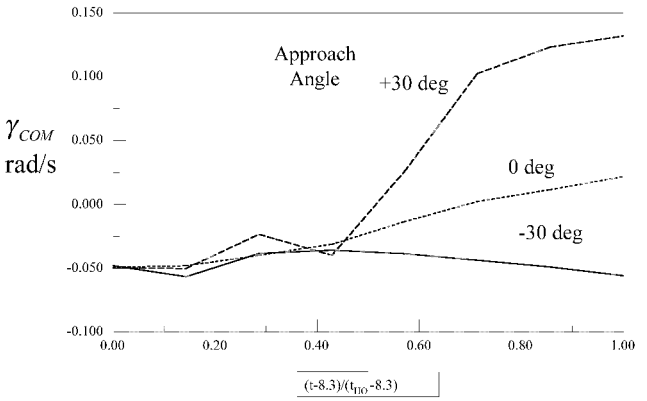

Fig. 8 Optimal commanded flight-path angle rate histories.

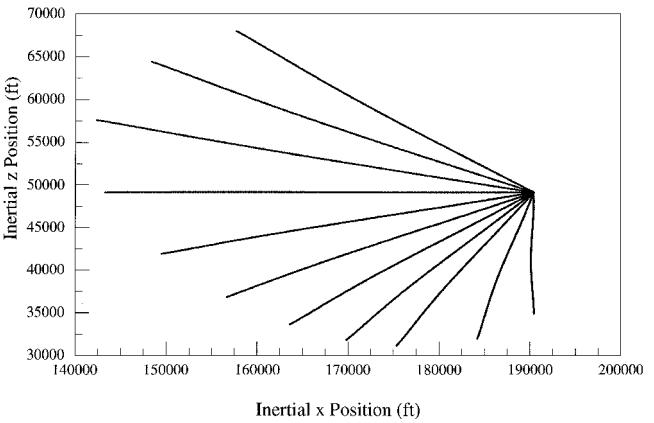

Fig. 9 Nominal second-tier trajectories to stationary PIP.

The handover states in Table 3 are used to initialize the second-tier terminal phase model. The second-tier phase of the trajectories associated with the nominal flyout to the stationary PIP without error sources are shown in Fig. 9. The final and handover velocities associated with the nominal flights to the stationary PIP are shown in Fig. 10. The plot indicates that an approach angle of approximately −10 deg maximizes both the handover and final speed. Although this approach angle maximizes the final speed, the results against the dynamic second-tier target will show that this approach does not necessarily maximize the overall system performance.

The second-tier trajectories against the 2-g maneuvering target in the absence of targeting errors are shown in Fig. 11. Here the

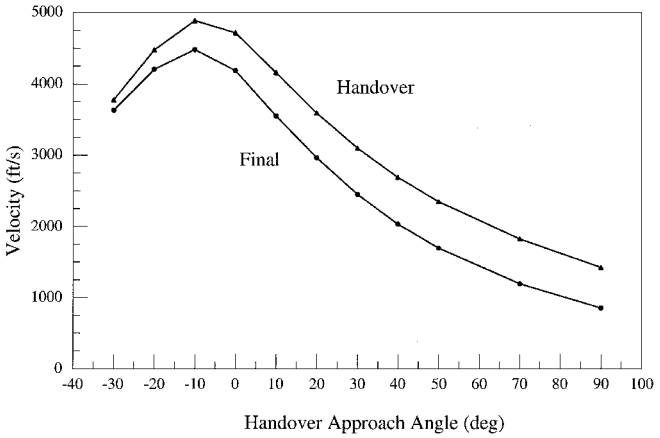

Fig. 10 Velocities against stationary PIP.

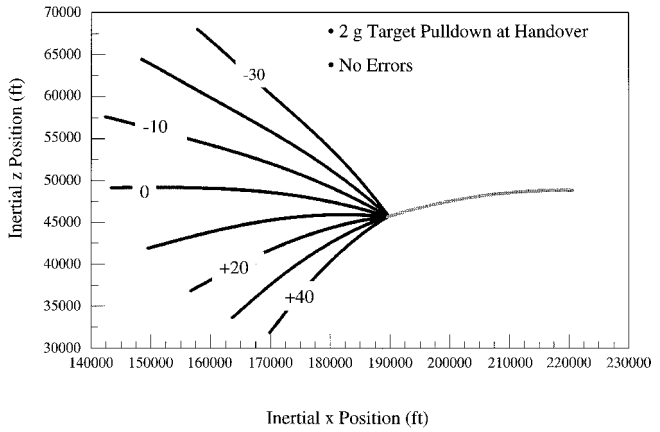

Fig. 11 Trajectories against maneuvering target.

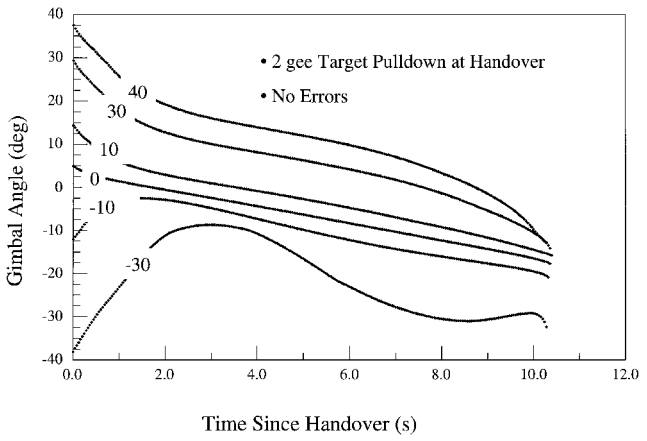

Fig. 12 Gimbal history against maneuvering target.

target maneuver begins at the handover time. Unlike the static PIP target, the intercepts points vary along the target trajectory. The intercept launch inertial x positions vary over approximately 400 ft, with the −30-deg approach angle intercepting at the greatest range. As the approach angle becomes more positive, the intercept launch inertial x position decreases until an approach angle of +10 deg. As the approach angle becomes steeper, the intercept position moves toward greater values of the launch inertial x position. Against the dynamic target, intercepts greater 40 deg are not possible because the speed of the target requires gimbal angles in excess of 45 deg.

The gimbal angles associated with the feasible intercepts are shown in Fig. 12. The gimbal angle magnitudes are greatest at the beginning of the terminal homing phase and are greatest for the two extreme approach angles of −30 and +40 deg. For the diving

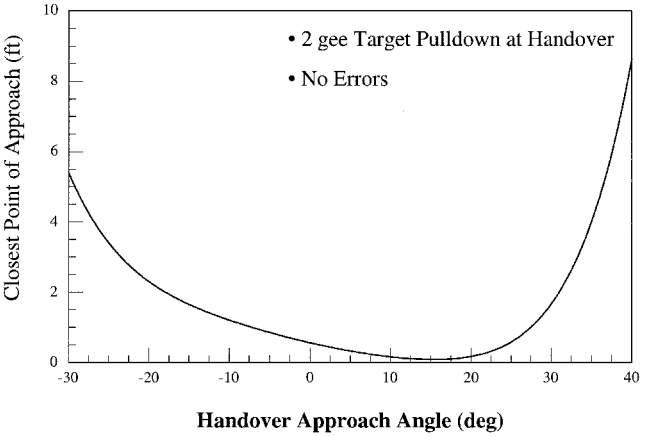

Fig. 13 Deterministic miss against maneuvering target.

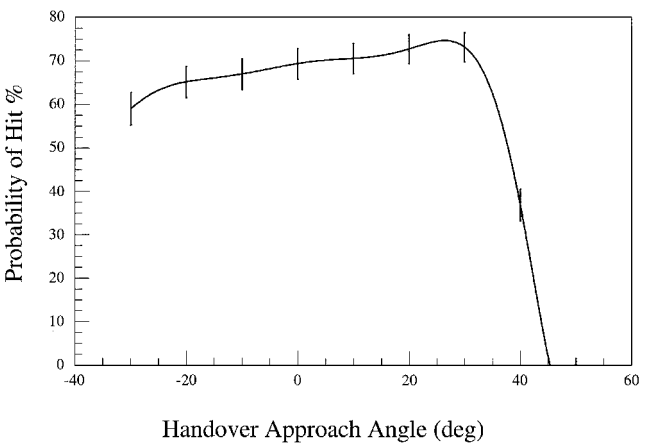

Fig. 14 Stochastic performance with nonmaneuvering target.

approach angles (negative values), the gimbal angle magnitude reaches a minimum early in the second-tier trajectory and then increases as the time to go to the intercept decreases.

The deterministic miss distance values against the 2-g diving target maneuver initiated at handover are shown in Fig. 13. The targeting error sources in the second-tier Monte Carlo modeling have not been included in this analysis. A positive approach angle between +10 and +20 deg minimizes the miss distance against the target. This result stands in contrast to the approach angle of −10 deg that maximizes the final and handover missile speeds. These results indicate that a simple relationship between missile speed and terminal homing performance does not exist. While the positive approach angle sacrifices speed at handover, the lower altitude at handover provides greater atmospheric density that serves to compensate for the reduced speed in terms of dynamic pressure and resultant missile maneuverability.

The next step in the analysis is to activate all of the error sources for the second tier simulation. These include 1) radome boresight error, 2) range-dependent noise on the rf semiactive seeker, 3) glint angular noise off of the target, and 4) the heading error at handover. The Monte Carlo analysis used 500 trials in determining the probability of hit. The results against the nonmaneuvering target are shown in Fig. 14. The error bars in Fig. 14 indicate the 90% confidence interval. Here the target maintains a constant altitude at a velocity of 3000 ft/s. As the approach angle steepens, the probability of hit increases. The performance is maximized at an approach angle of +30 deg. For larger approach angles, the gimbal angle limit becomes active and destroys the homing performance.

The benefit of the steeper approach angle derives from the contribution of the range-dependent receiver noise to the final miss distance. In the absence of target maneuver, the glint, the boresight error effects, and the range-dependent noise drive the miss. The steeper approach angles have lower closing velocity values than the

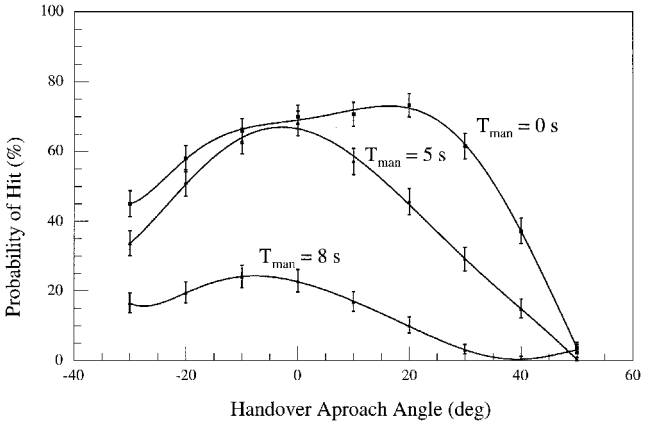

Fig. 15 Stochastic performance with target maneuvers.

0-deg approach angle. The lower closing velocities lessen the impact of receiver noise on the miss distance. The steeper climbing approach angle trajectories have longer time constants at the end of the flight as compared to the diving approach angles. The longer time constants increase the impact of receiver noise while decreasing the effect of radome boresight error slope and target glint. These conflicting trends must be resolved through numerical simulation.

The impact of target maneuver is now considered for the stochastic scenario. Once again, a 2-g target pulldown is considered. Figure 15 shows the probability of hit results for three target maneuver times. One is at the initiation of the terminal homing phase ($T_{\text{man}} = 0$ s). This represents a pulldown to engage a surface point. For this maneuver, the probability of hit is maximized for an approach angle of +20 deg. Here performance is maximized by the use of the steeper climbing trajectories, which provide smaller time constants during the initiation of the maneuver and which provide greater interceptor divert capability because of the higher dynamic pressure values present during the first half of the terminal phase. Because of the long time of the target maneuver for this case, this additional divert capability in the interceptor is important.

For a maneuver starting during the middle of the terminal homing phase ($T_{\text{man}} = 5$ s), the probability of hit is maximized for an approach angle of 0 deg. Performance against this maneuver is optimized by a trajectory that balances the initial time constant and dynamic pressure with their respective values near the end of the terminal homing phase.

Finally, the late maneuver ($T_{\text{man}} = 8$ s) is considered. For this case, the −10-deg approach angle trajectory maximizes the probability of hit, which is also the approach angle that maximizes the missile velocity at the intercept. This trajectory has greater dynamic pressure available at the end of the trajectory when the maneuver is initiated. Because the maneuver time of the target is limited the need for total divert capability of the interceptor is diminished.

Conclusions

A method was presented whereby the midcourse trajectory of a surface-to-air missile was optimized to maximize the probability of hit against the target. A two-tier approach to the design was used. The first tier represented the midcourse trajectory of the missile, and the second phase represented the terminal homing phase. The first-tier trajectory was optimized with an auxiliary constraint beyond the constraints native to the problem. The auxiliary constraint was defined as an equality constraint on the value of the approach angle to the intercept at handover to the terminal phase. The handover approach angle was used as the governing parameter in generating a field of optimum first-tier midcourse trajectories. The second-tier model was used to estimate the probability of hit with a full suite of error sources on the seeker and missile system. The first-tier trajectory and its associated approach angle that maximized the probability of hit were selected as the best choice for maximizing the final end-to-end performance.

The optimal approach angle was not necessarily the value that maximized the final velocity at intercept. The optimal value is determined by the type and magnitude of errors present in the missile and by the assumed target behavior. Against the nonmaneuvering target, the +30-deg approach angle was found to be optimal. Against the target that performs a 2-g pulldown, the optimal approach angle varied from +20 to −10 deg as the initiation time of the maneuver was delayed.

The method presented demonstrates connectivity between the midcourse trajectory design and the terminal homing guidance performance. Improved performance may be possible by a method that allows terminal homing performance measures of effectiveness in the midcourse trajectory optimization. The auxiliary approach angle constraint presented provides one such approach.

Appendix A: Thrust and Aerodynamic Models

For both tiers, the thrust is computed by

$$T = T_{\text{sl}} + A_e(p - p_{\text{sl}}), \qquad A_e = 0.2453 \text{ ft}^2 \tag{A1}$$

The weight varies linearly in time during the second stage motor burn between the initial value of the second stage of the missile and its burnout weight as given in Table 1.

In the first-tier simulation/optimization model, maintaining smoothness in the aerodynamic evaluation is paramount. The aerodynamics are modeled with a drag polar of the form

$$C_D = C_{D0} + KC_L^2 \tag{A2}$$

The data for the drag polar are interpolated in Mach number by the use of a cubic spline through the data given in Table A1. In the first-tier model during the motor burn, the value of C_{D0} is reduced by 0.15 for Mach numbers less than or equal to 4.0 and 0.1 for higher Mach numbers.

The following relation estimates the angle of attack:

$$\alpha = (C_L / C_{L\max})\alpha_{\max} \tag{A3}$$

The maximum angle of attack is 25 deg for both tiers. In the first tier, the maximum lift coefficient is applied as a constraint during the trajectory optimization as indicated in Eq. (16). A cubic spline is fit through the data in Table A2 to allow interpolation in Mach number.

Table A1 First-tier trim aerodynamic model

Mach number	C_{D0}	K
0.0	0.64	0.071
0.8	0.70	0.065
0.9	0.86	0.062
1.1	1.05	0.053
1.2	1.10	0.051
1.3	1.12	0.050
1.5	0.93	0.051
2.0	0.77	0.057
3.0	0.57	0.071
5.0	0.39	0.080
6.0	0.30	0.085

Table A2 First-tier maximum lift coefficient

Mach number	$C_{L\max}$
0.0	6.6
0.9	7.4
1.3	9.4
1.5	9.2
2.0	8.2
3.0	6.5
5.0	5.8
6.0	5.5

Without the requirement of smoothness in the second-tier model, creation of a higher fidelity aerodynamic modeling is easily accomplished. The axial force coefficient is created by a component buildup approach:

$$C_A = C_{D0} - \Delta C_{DB} + \Delta C_{Dh} + \Delta C_{DA} \tag{A4}$$

The zero-lift axial coefficient value at sea level (after motor burnout) is determined by linear interpolation in Mach number on the C_{D0} data in Table A1. The base drag reduction term ΔC_{DB} is zero after motor burnout. When the motor is burning, the data in Fig. A1 are linearly interpolated with respect to Mach number.

An increment is added to reflect the greater viscous drag effects at higher altitudes as a function of the Mach number and the altitude. The data in Figs. A2 and A3 are linearly interpolated in Mach number and altitude to compute the increment.

The increased angle of attack results in changes in the axial coefficient. This increment is computed by linear interpolated of Mach number and angle of attack from the data in Figs. A4 and A5.

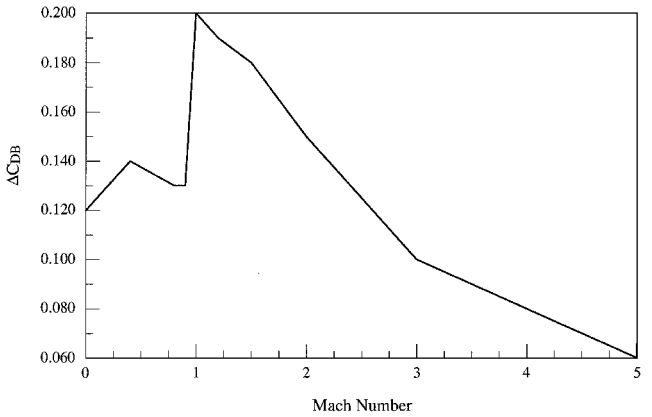

Fig. A1 Base drag reduction coefficients.

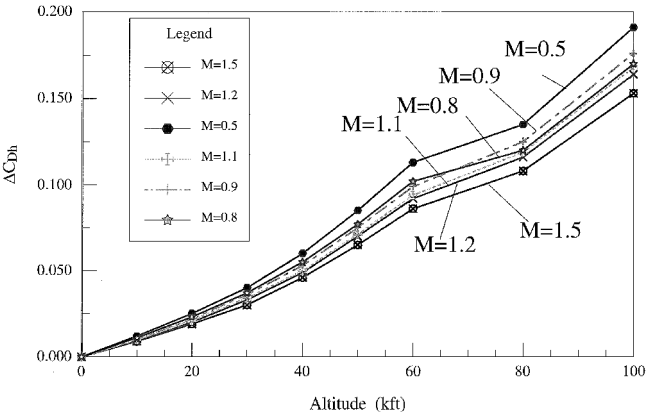

Fig. A2 Altitude axial coefficient increments (low Mach).

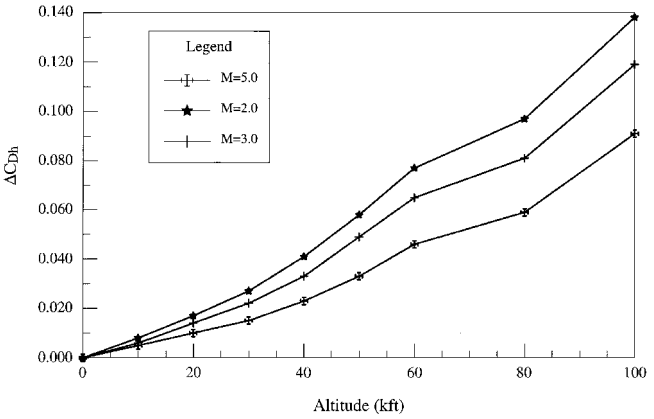

Fig. A3 Altitude axial coefficient increments (high Mach).

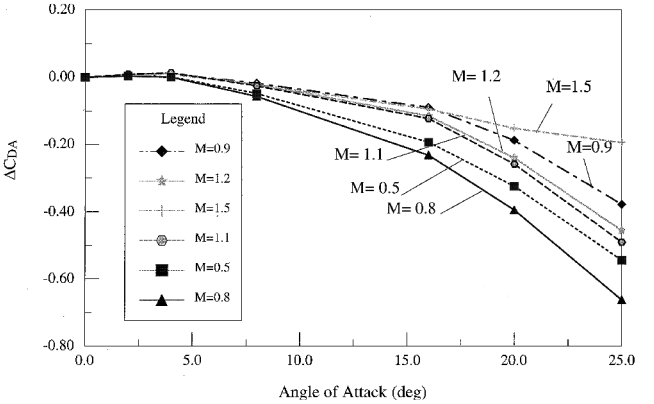

Fig. A4 Angle-of-attack axial coefficient increments (low Mach).

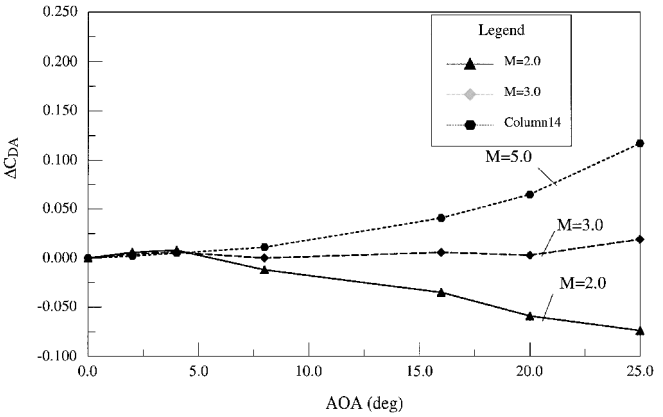

Fig. A5 Angle-of-attack axial coefficient increments (high Mach).

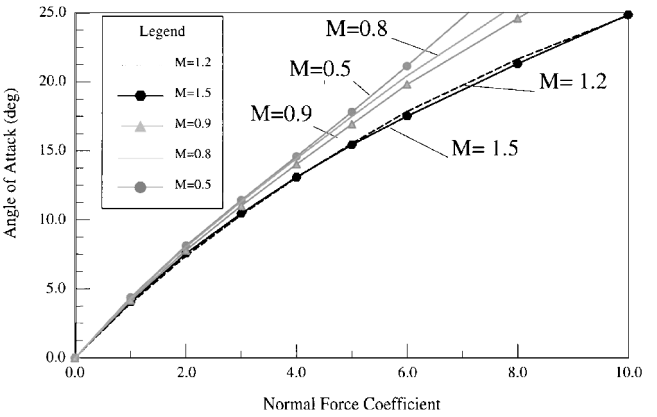

Fig. A6 Trim angle-of-attack values (low Mach).

The angle of attack used for the axial force coefficient computations is a function of the specific force along the body z axis from the first-order airframe model:

$$C_N = a_{zB}/qS_{\text{ref}} \tag{A5}$$

The angle of attack associated with this normal force coefficient is computed through linear interpolation on trim aerodynamic data in terms of the normal coefficient and the Mach number. The data are presented in Figs. A6 and A7. In the second-tier simulation, the data in maximum normal force coefficient is interpolated as a function of Mach number and applied as a limit to the achieved normal force coefficient. The numerical values of the maximum normal force coefficient may be obtained from Figs. A6 and A7 for the maximum allowable angle of attack of 25 deg.

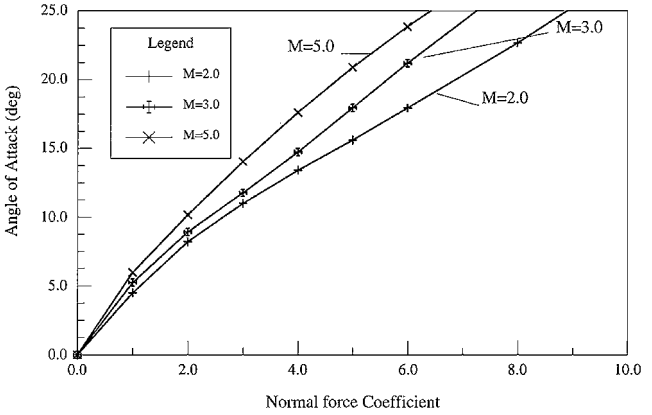

Fig. A7 Trim angle-of-attack values (high Mach).

Appendix B: Autopilot/Airframe Time Constant Scheduling

The autopilot/airframe time constant is scheduled as a function of the flight conditions. The minimum autopilot time constant is determined by ensuring the stability of the missile-normal-specific-force to target line-of-sight-rate transfer function in the presence of radome boresight error slope. The transfer function is given as

$$\frac{a_{zB}}{\hat{\xi}} = \frac{K_g}{A_3 s^3 + A_2 s^2 + A_1 s + A_0}, \qquad A_3 = \tau_A + \tau_N + \tau_S$$

$$A_2 = \tau_A \tau_N + \tau_A \tau_S + \tau_N \tau_S, \qquad A_1 = \tau_A + \tau_N + \tau_S + K_0 r_{\text{bes}} \tau_q$$

$$A_0 = 1 + K_0 r_{\text{bes}}, \qquad \tau_N = \frac{\delta t}{\log(1 - \alpha_N)}$$

$$\tau_q = \frac{mV}{q S_{\text{ref}} C_{N\alpha}}, \qquad K_0 = \frac{K_g}{V} \tag{B1}$$

The stability of the transfer function in Eq. (B1) is controlled by solving for the value of τ_A that allows the denominator to satisfy Routh's criterion. The value of r_{bes} is set at the worst-case specified value of -0.08. The value of $C_{N\alpha}$ used in Eq. (B1) is the local slope as determined by numerical differentiation of the data in Figs. A6 and A7 over a small step in angle of attack for the current Mach number. Application of Routh's criterion leads to the following requirement:

$$A_2 A_1 - A_3 A_0 > 0 \tag{B2}$$

This approach yields a quadratic equation in τ_A. This algorithm is computed throughout the terminal homing engagement to adaptively set the autopilot time constant. In an approximate sense, the requirement on the autopilot time constant may be expressed as

$$\tau_A > -\tau_s - \tau_N - K_0 r_{\text{bes}} \tau_q \tag{B3}$$

For negative values of r_{bes}, there will be a minimum value of the autopilot time constant to ensure stability. At high altitudes, where τ_q can grow to large values, the effective time constant can grow large to ensure stability in the presence of radome boresight error slope.

The autopilot time constant determined from Eq. (B2) is subject to an additional minimum value as a function of the dynamic pressure. This constraint represents the limit of performance given the specified actuator bandwidth and desired operating range. This dynamic pressure scheduling is given by

$$\tau_{A\min} = 10 q^{0.2} \tag{B4}$$

Acknowledgments

Ernest Ohlmeyer of the Naval Surface Warfare Center first suggested the tiered concept of trajectory optimization and developed the terminal homing model. Also, Eugene Cliff of the Virginia Polytechnic Institute and State University provided many keen observations of the method as J. C. Drake's Independent Research Advisor. The Associate Editor, Frederick Lutze, and the reviewers provided extensive commentary to clarify the paper.

References

[1] Adler, P., "Missile Guidance by Three-Dimensional Proportional Navigation," *Journal of Applied Physics*, Vol. 27, No. 5, 1956, pp. 500–507.

[2] Nesline, F. W., and Zarchan, P., "A New Look at Classical vs Modern Homing Missile Guidance," *Journal of Guidance, Control, and Dynamics*, Vol. 4, No. 1, 1981, pp. 78–85.

[3] Nesline, F. W., and Zarchan, P., "Miss Distance Dynamics in Homing Missiles," AIAA Paper 84-1844, Aug. 1984.

[4] Chadwick, W. R., "Miss Distance of Proportional Navigation Missile with Varying Velocity," *Journal of Guidance, Control, and Dynamics*, Vol. 8, No. 5, 1985, pp. 662–666.

[5] Murtaugh, S. A., and Criel, H. E., "Fundamentals of Proportional Guidance," *IEEE Spectrum*, Dec. 1966, pp. 75–85.

[6] Zarchan, P., "When Bad Things Happen to Good Missiles," *Proceedings of the AIAA Guidance, Navigation, and Control Conference*, AIAA, Washington, DC, 1993, pp. 765–773.

[7] Phillips, C., "Terminal Homing Performance of Semiactive Missiles Against Multitarget Raids," *Journal of Guidance, Control, and Dynamics*, Vol. 18, No. 6, 1995, pp. 1427–1433.

[8] Kelley, H. J., and Speyer, J. L., "Accelerated Gradient Projection," *Lecture Notes in Mathematics*, Vol. 132, Springer-Verlag, Berlin, 1970.

F. H. Lutze Jr.
Associate Editor